Volume 13
Number 42
14 November 2025
Pages 35907–36760

Journal of Materials Chemistry A

Materials for energy and sustainability

rsc.li/materials-a

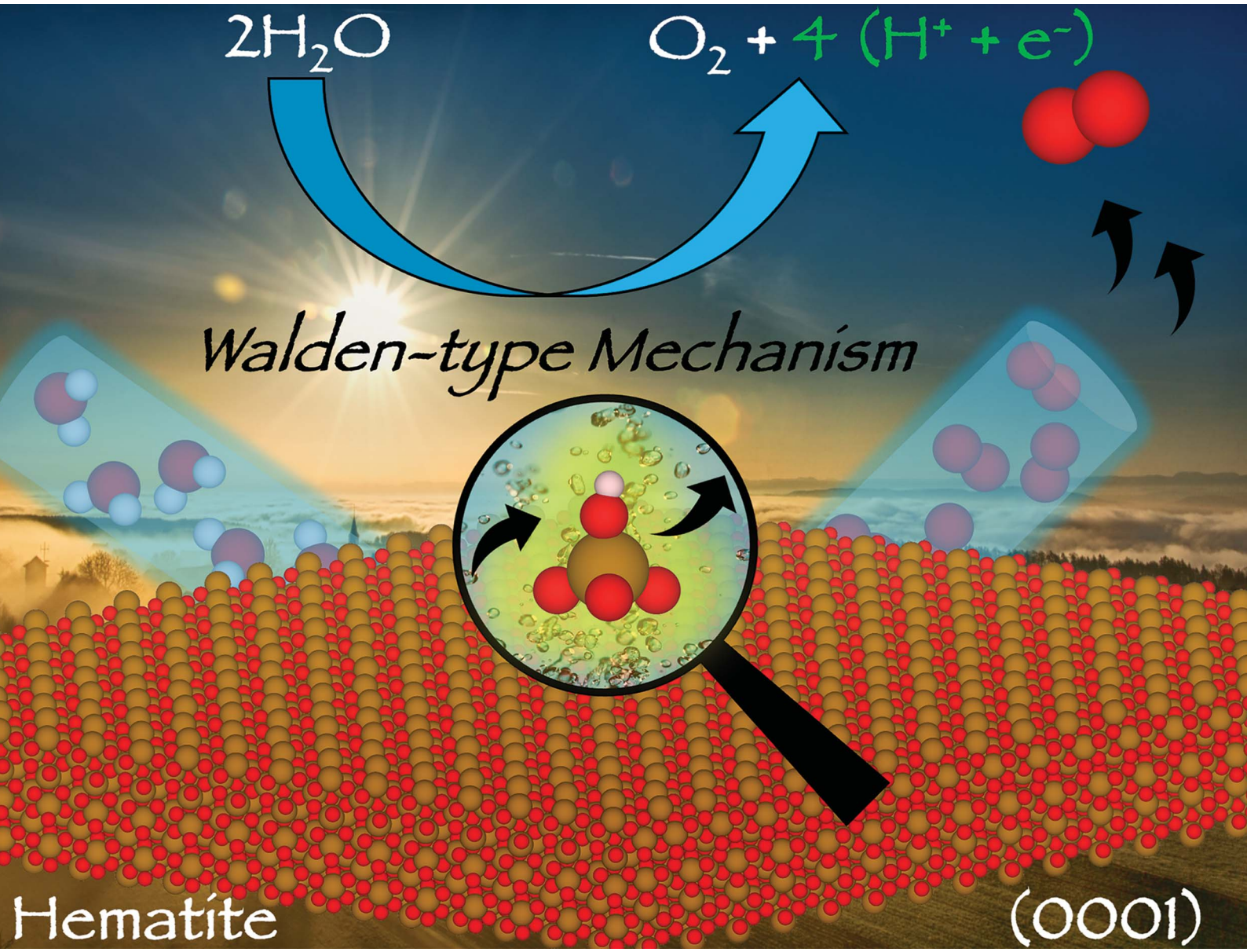

ISSN 2050-7488

ROYAL SOCIETY OF CHEMISTRY

PAPER

Kai S. Exner *et al.*

Atomic-scale insights into the oxygen evolution reaction on hematite: a detailed mechanistic investigation of different surface coverages

Journal of Materials Chemistry A

ROYAL SOCIETY OF CHEMISTRY

PAPER

View Article Online
View Journal | View Issue

Cite this: J. Mater. Chem. A, 2025, 13, 36104

Atomic-scale insights into the oxygen evolution reaction on hematite: a detailed mechanistic investigation of different surface coverages

Shinie S. Awulachew, [a] Kapil Dhaka, [a] Ebrahim Tayyebi[a] and Kai S. Exner *[abc]

The oxygen evolution reaction (OER)—$2H_2O \rightarrow O_2 + 4H^+ + 4e^-$—is the limiting half-cell reaction in the electrochemical water splitting process for the production of green hydrogen. In photoelectrochemical cells for solar water splitting, hematite (α-Fe_2O_3) is among the state-of-the-art anode materials. Despite extensive research, the mechanistic understanding of the OER on hematite is still incomplete, and previous computational work suggested that the less stable Fe–Fe–O–, rather than the most stable Fe–O–Fe– surface termination of α-Fe_2O_3(0001), is responsible for its high OER activity. Using a comprehensive density functional theory framework, we investigate seven different OER mechanisms for five different surface coverages of the most stable Fe–O–Fe– surface termination and find that the OER preferentially proceeds *via* Walden-type mechanisms that have been overlooked in previous work. The present contribution advances the understanding of OER mechanisms on hematite, emphasizing the importance of considering multiple pathways in the analysis of the elementary steps, and proposes to exploit the most stable Fe–O–Fe– termination for the development of advanced hematite-based photoanodes.

Received 11th June 2025
Accepted 18th August 2025

DOI: 10.1039/d5ta04755b

rsc.li/materials-a

1 Introduction

Water electrolysis is a key process for a sustainable energy scenario without dependence on fossil fuels.[1] Over the last decade, considerable efforts have been made to develop catalyst materials for electrochemical or photoelectrochemical (PEC) conditions, with hematite (α-Fe_2O_3) being a promising material for the sluggish oxygen evolution reaction (OER)—$2H_2O \rightarrow O_2 + 4H^+ + 4e^-$, $U^0 = 1.23$ V *vs.* reversible hydrogen electrode (RHE)—at the anode of a PEC device.[2] α-Fe_2O_3 has a favorable band gap of approximately 2.1 eV,[3–13] which lies in the visible range of the electromagnetic spectrum, is stable in aqueous environments and is abundant in nature.[2] Although hematite has been investigated in several previous works using experimental and theoretical approaches for OER,[2,6–22] there are still open issues that need to be addressed, including low hole mobility,[23,24] high recombination rates, or short lifetimes of photogenerated electron–hole pairs.[25]

Despite the remarkable progress in the field, even the most optimal ultrathin hematite films exhibit a substantial overpotential of 0.5–0.6 V for the OER to reach a current density of at least 1 mA cm^{-2}.[2,15,20,26,27] This experimental overpotential was explained in previous computational studies using the concept of the thermodynamic overpotential according to Nørskov's approach[6–13] and by focusing on the most common (0001) surface of hematite.[7,10,12–14,16–18,28–31] Liao *et al.* estimated a thermodynamic overpotential of 0.77 V for the OER on a hydroxylated α-Fe_2O_3(0001) surface, which is qualitatively comparable with the experimental overpotential for a current density of at least 1 mA cm^{-2}.[13]

On the other hand, it has to be noted that previous theoretical works suggested that the Fe–Fe–O– rather than the most stable Fe–O–Fe– termination of hematite is responsible for its catalytic activity in the OER. This statement is based on activity predictions using the thermodynamic overpotential: for instance, Nguyen *et al.*[12] determined a relatively high value of 1.22 V for the most stable Fe–O–Fe– termination, while the second most stable Fe–Fe–O– termination yielded a thermodynamic overpotential of 0.84 V, which is closer to the experimental overpotential. This result is in qualitative agreement with a study by Hajiyani and Pentcheva,[10] who reported thermodynamic overpotentials of 1.12 V and 0.81 V for the Fe–O–Fe– and Fe–Fe–O– terminations, respectively. In addition, it was demonstrated that the introduction of hydrogen into the less stable Fe–Fe–O– surface termination reduced the thermodynamic overpotential to 0.56 V, thus purporting that the Fe–Fe–O– termination rather than the most stable Fe–O–Fe– termination might be reconciled with the active phase in the OER on hematite.

Although previous computational studies on the (0001) facet of hematite consistently show that the most stable Fe–O–Fe–

[a]University of Duisburg-Essen, Faculty of Chemistry, Theoretical Catalysis and Electrochemistry, Universitätsstraße 5, 45141 Essen, Germany. E-mail: kai.exner@uni-due.de
[b]Cluster of Excellence RESOLV, 44801 Bochum, Germany
[c]Center for Nanointegration (CENIDE) Duisburg-Essen, 47057 Duisburg, Germany

surface termination is inactive for OER, we challenge this finding in the present manuscript by overcoming the limitations of previous work. In this context, we emphasize that all previous computational studies relied on the consideration of a single mechanism—the mononuclear description[32]—although mechanistic diversity in OER has been shown to be relevant, especially for active OER materials.[33,34] In addition, the previous works are based on the application of the thermodynamic overpotential as the activity descriptor for electrocatalytic activity, although it has been shown that several elementary reaction steps can contribute to the reaction rate to varying degrees.[35] Finally, surface coverage has been largely ignored or not consistently described in previous work, although the presence of different adsorbate species on the hematite surface can influence the energetics of the elementary reaction steps.

In the present work, we investigate the OER on the Fe–O–Fe– surface termination of α-Fe_2O_3(0001) surface by incorporating a variety of different mechanistic pathways into the analysis of the elementary steps and by applying the $G_{max}(U)$ descriptor based on the energetic span model[36] as a measure for the electrocatalytic activity. Using this dedicated computational protocol, we solve the elementary steps of the OER on α-Fe_2O_3(0001) for different surface coverages based on a careful sampling using Pourbaix diagrams. We demonstrate that, contrary to previous literature studies, the Fe–O–Fe– termination of hematite is active in the OER and catalyzes the formation of gaseous oxygen by non-conventional Walden mechanisms.[34,37,38]

2 Theoretical model

To investigate the oxygen evolution reaction (OER) on α-Fe_2O_3(0001), we perform electronic structure calculations within the framework of density functional theory (DFT) using the Vienna *Ab initio* Simulation Package (VASP).[39–41] To account for the localized nature of the Fe 3d electrons, a Hubbard U correction of 4.2 eV is applied.[42–44] The VASPsol extension is used to describe the aqueous electrolyte at the solid/liquid interface.[45] The Perdew–Burke–Ernzerhof (PBE) functional[46] was used, and we incorporated on-site Coulomb interactions through a Hubbard U correction (PBE + U),[47] with an effective Coulomb repulsion parameter usually chosen between 4.0–4.3 eV (ref. 42 and 43) for the d-electron states of iron. In our calculations, U was set to at 4.2 eV, resulting in a band gap of 2.0 eV, which is in agreement with previous studies.[6,12,17,42,43] Grimme's D3 dispersion correction[48] was included to correct the obtained energetics for dispersion effects. To minimize interactions between periodic images, a vacuum gap of at least 16 Å is included along the surface normal direction. Furthermore, due to the use of an asymmetric slab model, a dipole correction was applied perpendicular to the surface (along the z-direction) to eliminate spurious interactions between periodic images.[49] To account for the effects of core electrons on the valence electron density, the projector augmented wave (PAW) method[50] was used. The number of valence electrons considered for Fe and O corresponds to 14 and 6. The Gaussian smearing method is used to optimize the atomic structure with a smearing width of 0.05 eV. The convergence criterion for forces and total energy along the self-consistent field (SCF) is set to 0.01 eV $Å^{-1}$ and 10^{-6} eV, respectively. The ASE software[51] and VESTA software[52] are used to visualize and construct the unit cell and slab models. Further computational details are provided in Section S1 of the SI. There, the magnetic configurations of hematite in the primitive unit cell are discussed and the corresponding surface models based on the ground-state magnetic moment configuration are given in Section S2 of the SI. The modeling of electrochemical reaction steps using the computational hydrogen electrode (CHE) approach is described in Section S3 of the SI.

The OER is a complex process consisting of four proton-coupled electrons transfer steps to produce a single oxygen molecule. To gain insights into the elementary steps that occur under the harsh anodic reaction conditions ($U > 1.23$ V *vs.* RHE), analysis of various reaction mechanisms[35,53] is conducted by constructing free-energy diagrams along the reaction coordinate. Below, we provide an overview of the mechanistic processes by categorizing them into single-site and dual-site OER mechanisms.

2.1 Single-site OER mechanisms

We consider two single-site mechanisms, namely the well-established mononuclear mechanism[54,55] and a Walden-type description of this pathway, in which adsorption and desorption occur in a concerted manner.[34,38,56]

2.1.1 Mononuclear mechanism. This mechanism involves the sequential oxidation of water to form the *OH, *O, and *OOH intermediates on a single active site:[54,55]

$$* + H_2O_{(l)} \rightarrow *OH + (H^+ + e^-),\ \Delta G_1 \quad (1)$$

$$*OH \rightarrow *O + (H^+ + e^-),\ \Delta G_2 \quad (2)$$

$$*O + H_2O_{(l)} \rightarrow *OOH + (H^+ + e^-),\ \Delta G_3 \quad (3)$$

$$*OOH \rightarrow * + (H^+ + e^-) + O_{2(g)},\ \Delta G_4 \quad (4)$$

Note that the asterisk (*) denotes an active surface site of the electrocatalyst, such as a surface Fe atom in α-Fe_2O_3(0001) of the Fe–O–Fe– surface termination (*cf.* Fig. 1a).

2.1.2 Mononuclear-Walden mechanism. This mechanism represents a modified version of the mononuclear pathway. Compared to the conventional description, the *OOH adsorbate is first oxidized to *OO and the desorption of *OO is accompanied by its replacement by water from the solution, which is oxidized to form *OH (*cf.* eqn (7) and (8)):

$$*OH \rightarrow *O + (H^+ + e^-),\ \Delta G_5 \quad (5)$$

$$*O + H_2O_{(l)} \rightarrow *OOH + (H^+ + e^-),\ \Delta G_6 \quad (6)$$

$$*OOH \rightarrow *OO + (H^+ + e^-),\ \Delta G_7 \quad (7)$$

$$*OO + H_2O_{(l)} \rightarrow *OH + (H^+ + e^-) + O_{2(g)},\ \Delta G_8 \quad (8)$$

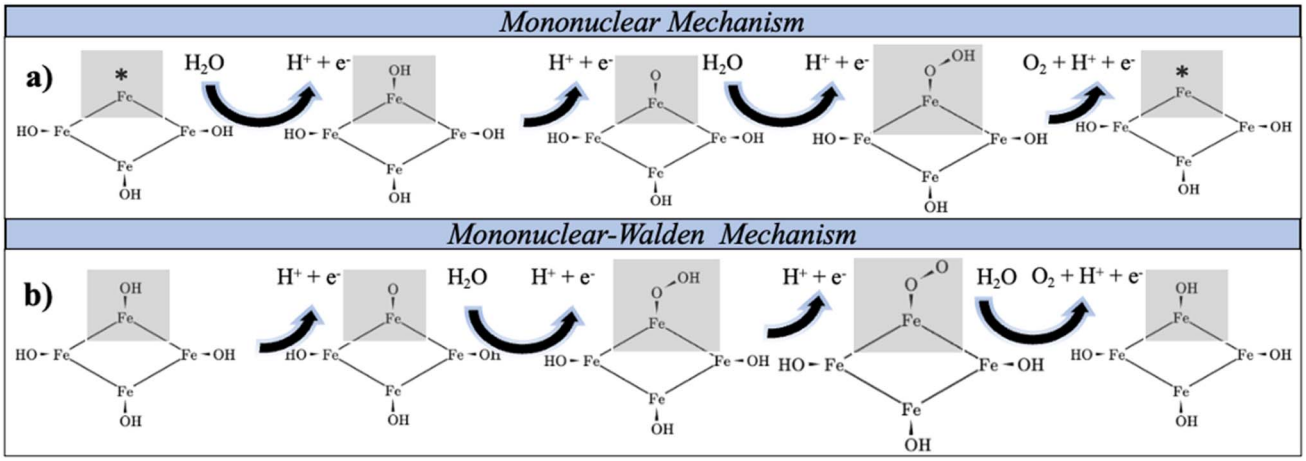

Fig. 1 Schematic representation of single-site OER mechanisms over Fe_2O_3(0001) based on a sketch for the α-Fe_2O_3(0001)-4*OH surface (top view) with active sites highlighted in gray color: (a) mononuclear mechanism, starting from a partially *OH-covered surface; (b) mononuclear-Walden mechanism, starting from a fully *OH-covered surface with a concerted desorption–adsorption step.

2.2 Dual-site OER mechanisms

In addition to the single-site OER mechanism, it is also possible to form gaseous oxygen *via* multi-site pathways, where the availability of multiple active sites opens additional reaction channels.[57] Different forms of dual-site OER mechanisms are described below, although it is important to note that the metal sites are too far apart to interact directly. However, a single iron atom in hematite can bind several adsorbates, resulting in branching behavior (*cf.* Fig. 2). As a result, multiple adsorbates on the same iron atom are treated as functional equivalents of neighboring metal sites, thereby enabling dual-site mechanisms.

2.2.1 Bifunctional I mechanism. The bifunctional I mechanism requires two adjacent active sites to facilitate the formation of molecular oxygen. In this mechanism, the second site, represented by an oxygen adsorbate ($*O_A$) on the active iron center (*cf.* Fig. 2a), functions as a Brønsted base by accepting a proton–electron pair from a reacting water molecule (*cf.* eqn (11)). Consequently, the *OO intermediate rather than the *OOH adsorbate is formed.[58]

$$* + *O_A + H_2O_{(l)} \rightarrow *OH + *O_A + (H^+ + e^-),\ \Delta G_9 \quad (9)$$

$$*OH + *O_A \rightarrow *O + *O_A + (H^+ + e^-),\ \Delta G_{10} \quad (10)$$

$$*O + *O_A + H_2O_{(l)} \rightarrow *OO + *OH_A + (H^+ + e^-),\ \Delta G_{11} \quad (11)$$

$$*OO + *OH_A \rightarrow * + *O_A + (H^+ + e^-) + O_{2(g)},\ \Delta G_{12} \quad (12)$$

2.2.2 Bifunctional II mechanism. The bifunctional II mechanism[59–61] also incorporates a second site, $*O_A$, in its mechanistic description. However, it differs from the bifunctional I mechanism by including a chemical reaction step in the analysis (*cf.* eqn (15)). As a result, the bifunctional II mechanism consists of a total of five elementary steps.

$$* + *O_A + H_2O_{(l)} \rightarrow *OH + *O_A + (H^+ + e^-),\ \Delta G_{13} \quad (13)$$

$$*OH + *O_A \rightarrow *O + *O_A + (H^+ + e^-),\ \Delta G_{14} \quad (14)$$

$$*O + *O_A + H_2O_{(l)} \rightarrow *OOH + *OH_A,\ \Delta G_{15} \quad (15)$$

$$*OOH + *OH_A \rightarrow *OOH + *O_A + (H^+ + e^-),\ \Delta G_{16} \quad (16)$$

$$*OOH + *O_A \rightarrow * + *O_A + (H^+ + e^-) + O_{2(g)},\ \Delta G_{17} \quad (17)$$

2.2.3 Bifunctional-Walden mechanism. Similar to the mononuclear-Walden mechanism, the bifunctional-Walden mechanism modifies the final steps of the bifunctional I mechanism by considering a concerted adsorption–desorption step in the analysis (*cf.* eqn (21)):

$$*OH + *O_A \rightarrow *O + *O_A + (H^+ + e^-),\ \Delta G_{18} \quad (18)$$

$$*O + *O_A + H_2O_{(l)} \rightarrow *OO + *OH_A + (H^+ + e^-),\ \Delta G_{19} \quad (19)$$

$$*OO + *OH_A \rightarrow *OO + *O_A + (H^+ + e^-),\ \Delta G_{20} \quad (20)$$

$$*OO + *O_A + H_2O_{(l)} \rightarrow *OH + *O_A + (H^+ + e^-) + O_{2(g)},\ \Delta G_{21} \quad (21)$$

2.2.4 Binuclear mechanism. In the binuclear mechanism,[62,63] the formation of gaseous O_2 occurs by the chemical recombination of two adjacent oxygen adsorbates, which requires the presence of two neighboring metal sites (*cf.* eqn (26)):

$$* + * + H_2O_{(l)} \rightarrow *OH + * + (H^+ + e^-),\ \Delta G_{22} \quad (22)$$

$$*OH + * + H_2O_{(l)} \rightarrow *OH + *OH + (H^+ + e^-),\ \Delta G_{23} \quad (23)$$

$$*OH + *OH \rightarrow *O + *OH + (H^+ + e^-),\ \Delta G_{24} \quad (24)$$

$$*O + *OH \rightarrow *O + *O + (H^+ + e^-),\ \Delta G_{25} \quad (25)$$

$$*O + *O \rightarrow * + * + O_{2(g)},\ \Delta G_{26} \quad (26)$$

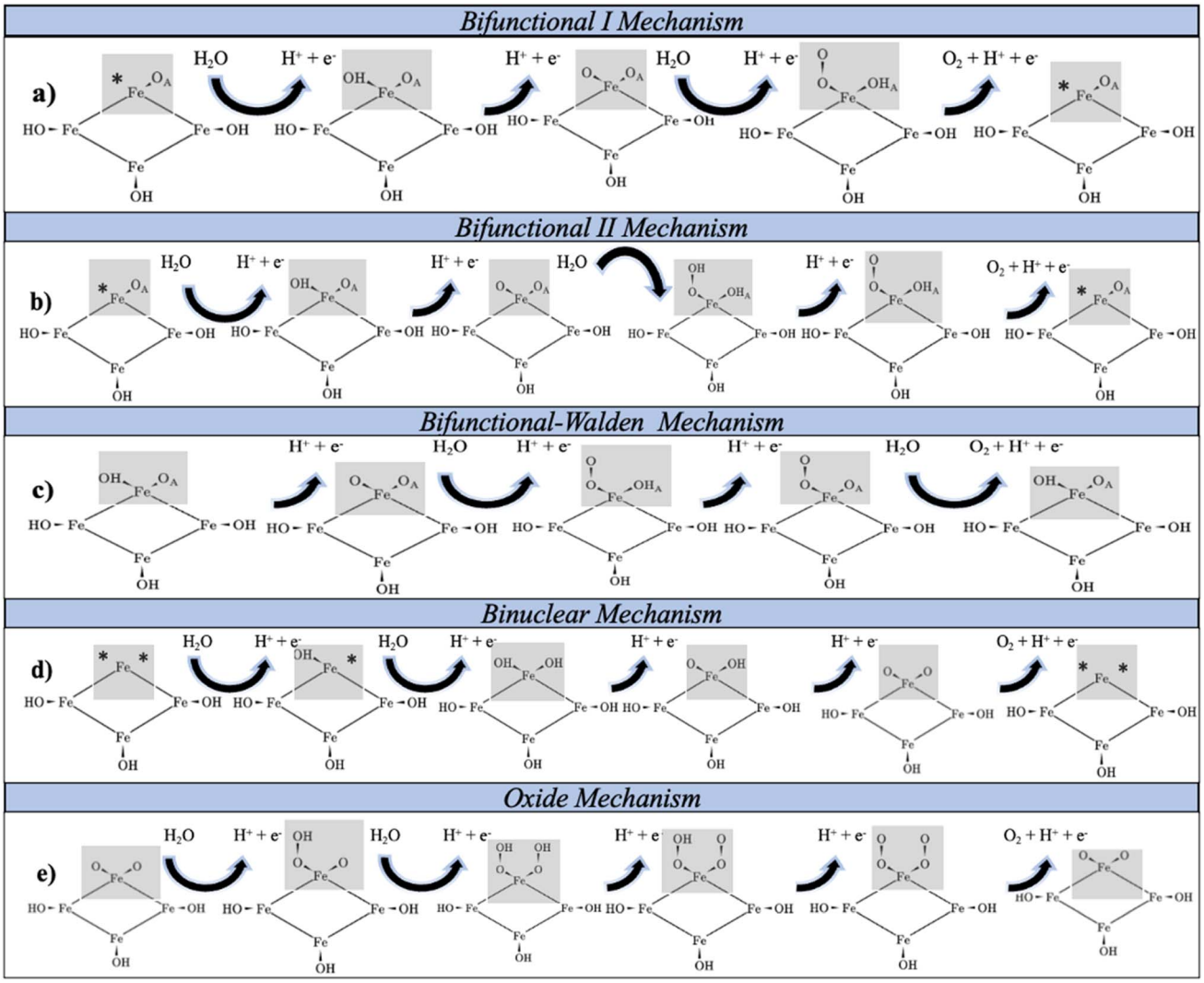

Fig. 2 Schematic representation of dual-site OER mechanisms over Fe_2O_3(0001) based on a sketch for the α-Fe_2O_3(0001)-4*OH surface (top view) with active sites highlighted in gray color: (a) bifunctional I mechanism; (b) bifunctional II mechanism; (c) bifunctional-Walden mechanism; (d) binuclear mechanism; (e) oxide mechanism.

2.2.5 Oxide mechanism. The oxide mechanism[64,65] is similar to the binuclear mechanism and involves two adjacent oxygen adsorbates facilitating the formation of gaseous O_2 by chemical recombination. The difference to the binuclear mechanism is that the outermost oxygen atoms of two adjacent *OO intermediates recombine, leaving one oxygen layer intact (*cf.* eqn (31)):

$$*O + *O + H_2O_{(l)} \rightarrow *OOH + *O + (H^+ + e^-),\ \Delta G_{27} \quad (27)$$

$$*OOH + *O + H_2O_{(l)} \rightarrow *OOH + *OOH + (H^+ + e^-),\ \Delta G_{28} \quad (28)$$

$$*OOH + *OOH \rightarrow *OOH + *OO + (H^+ + e^-),\ \Delta G_{29} \quad (29)$$

$$*OOH + *OO \rightarrow *OO + *OO + (H^+ + e^-),\ \Delta G_{30} \quad (30)$$

$$*OO + *OO \rightarrow *O + *O + O_{2(g)},\ \Delta G_{31} \quad (31)$$

Fig. 1 and 2 show the elementary steps of OER mechanisms considered in this study using α-Fe_2O_3(0001)-4*OH as a model surface. Note that the same analysis is conducted for all other relevant surface configurations based on the Pourbaix diagram of the Fe–O–Fe– surface termination (*cf.* Fig. S6).

2.3 Analysis of free-energy diagrams: activity descriptor $G_{max}(U)$

We construct free-energy diagrams using the CHE approach[66] for the mechanistic descriptions summarized in Sections 2.1 and 2.2 for different surface models of α-Fe_2O_3(0001) with different surface coverages (*cf.* Section 3). The resulting free-energy landscapes for these mechanistic descriptions are analyzed using the descriptor $G_{max}(U)$,[67] which represents the largest free-energy span among the free energies of the reaction intermediates.[25] While the most commonly used activity descriptor in the OER refers to the thermodynamic overpotential, η_{TD}, which extracts the largest free-energy change

within a given mechanistic description at the OER equilibrium potential by assuming that a single elementary step determines the reaction rate, the concept of $G_{max}(U)$ overcomes this limitation by allowing for the possibility that multiple elementary steps contribute to the reaction rate.[67] This is achieved through the notion of a span model,[68,69] which allows the evaluation of the potential-dependent descriptor $G_{max}(U)$ at any electrode potential and can lead to a change in the description of the limiting free-energy span with increasing driving force (*cf.* Fig. 3). A switch in the limiting span of $G_{max}(U)$ is therefore associated with a change in the rate-determining step, as often observed in experimental Tafel plots.[70,71] The inclusion of overpotential and kinetic effects in the thermodynamic descriptor $G_{max}(U)$ based on the adsorption free energies of the elementary steps goes far beyond the concept of η_{TD}, as further discussed in the literature.[72–75]

3 Results & discussion

3.1 Surface structure of α-Fe_2O_3(0001) under OER conditions

Water dissociates on hematite with very low energy barriers,[44] promoting the formation of *O, *OH, and/or *H surface species on the undercoordinated surface sites of the Fe–O–Fe– termination upon contact with water. We use a (2 × 2) unit cell for a α-Fe_2O_3(0001) slab model using the Fe–O–Fe– surface termination (*cf.* Fig. S3) to investigate the elementary steps of the OER. Note that the Fe–O–Fe– surface termination of α-Fe_2O_3(0001) was selected due to its stability under ambient temperature and pressure compared to other surface termination.[76,77] The concept of surface Pourbaix diagrams[78–80] is used to determine the surface coverage of α-Fe_2O_3(0001) under anodic polarization, which is explained in detail in Section S3 of the SI. The most stable surface coverages under (photo-)electrochemical conditions are shown in Fig. 4.

In the potential range relevant to OER, four different surface phases of α-Fe_2O_3(0001) turn out to be stable: (i) 4*OH & 4*H_{sub} for 1.00 V < *U vs.* RHE < 1.68 V; (ii) 4*OH for 1.68 V < *U vs.* RHE < 1.86 V *vs.* RHE; (iii) 8*OH for 1.86 V < *U vs.* RHE < 2.18 V *vs.* RHE; (iv) 12*O phase for *U vs.* RHE > 2.18 V *vs.* RHE. In addition to these four surface configurations, we consider the 4*OH & 4*O phase (*cf.* Fig. 4d) in our analysis, as it is energetically only slightly less stable than the 8*OH phase shown in the Pourbaix diagram (*cf.* Fig. S6). For the five different configurations of α-Fe_2O_3(0001), we model the elementary steps of the OER using seven different mechanistic descriptions (*cf.* Section 2 of the main text) to derive structure–activity relationships discussed below.

Please note that the (2 × 2) unit cell of α-Fe_2O_3(0001) consists of four Fe surface atoms, and each Fe atom can accommodate up to three adsorbates. Therefore, the elementary steps of the OER can occur either on a single branch or on multiple branches of an active Fe site. A single branch involves only one active adsorbate on the Fe site without co-adsorbates. In case of a double branch, one adsorbate is reactive while a second remains as a spectator. Similarly, a triple branch involves one reactive adsorbate and two spectator adsorbates on the same Fe site. For example, the 4*OH & 4*H_{sub} surface configuration can either catalyze the OER *via* a single branch or a double branch (with one *OH at the active site as a spectator). Please note that for the single branch, double branch, or triple branch of the active Fe site, single-site or dual-site OER mechanisms (*cf.* Section 2 in the main text) can proceed. These mechanisms may occur either independently of or in conjunction with the branching behavior, thereby broadening the spectrum of feasible OER pathways on the Fe–O–Fe– surface termination. For a dual-site OER mechanism requiring two active sites, a single-branch Fe active site uses a neighboring Fe atom (~5 Å away) to enable dual-site mechanisms. In contrast, for the double-branch and triple-branch Fe active sites, a single Fe atom can facilitate dual-site OER mechanisms due to the presence of multiple oxygen-containing adsorbates at the same active site (*cf.* Fig. 2). Possible branches for each surface coverage are summarized in Table 1.

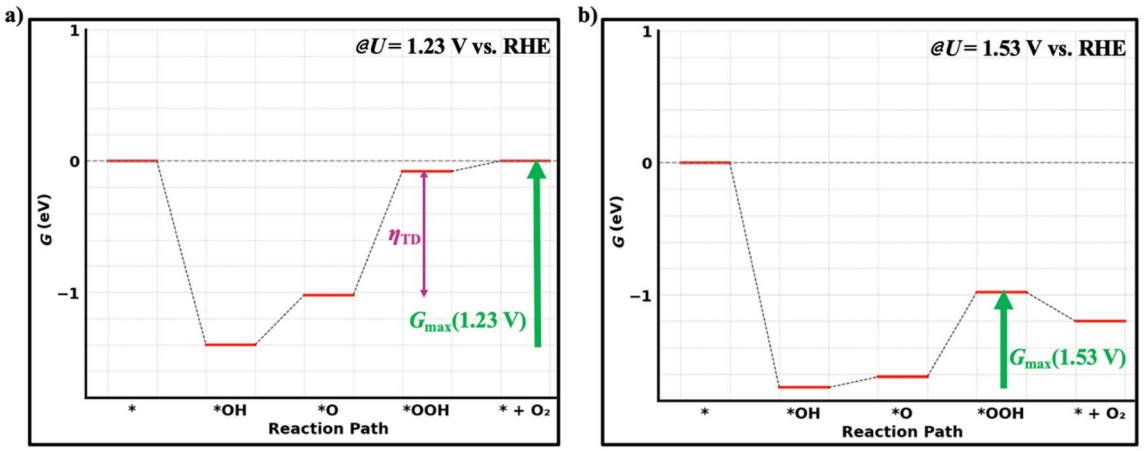

Fig. 3 (a) Arbitrary free-energy diagram of the OER at $U = 1.23$ V *vs.* RHE. The descriptor $G_{max}(U)$ is defined by the transition from the *OH to the * + O_2 state, while the thermodynamic overpotential (η_{TD}) is given by the transition from the *O to the *OOH intermediate. (b) Free-energy diagram of the OER at $U = 1.53$ V *vs.* RHE, corresponding to an applied overpotential of 300 mV. The descriptor $G_{max}(U)$ is defined by the transition from the *OH to the *OOH state, indicating a change in the limiting span.

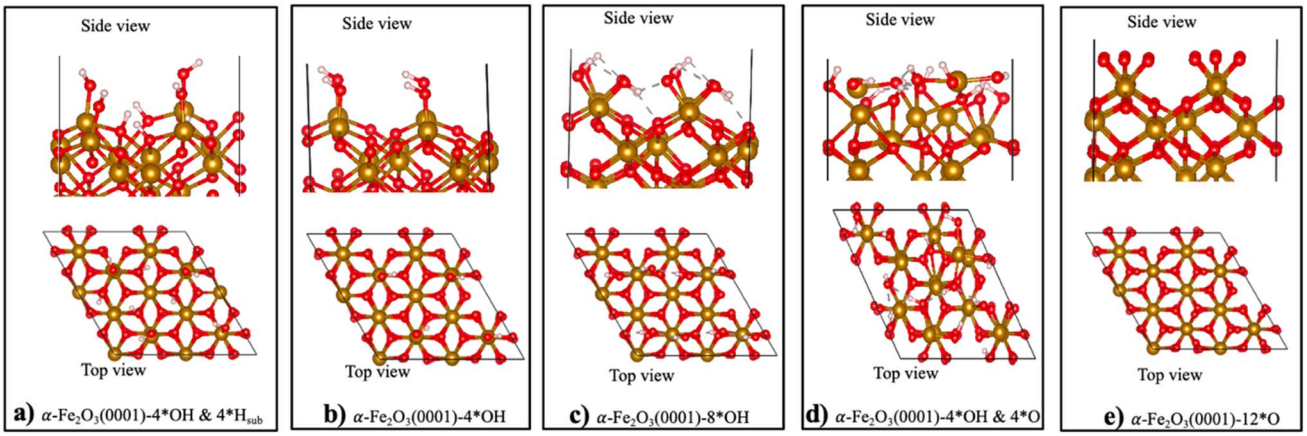

Fig. 4 Most stable surface coverages of α-Fe_2O_3(0001) on the Fe–O–Fe– surface termination for a (2 × 2) unit cell under (photo-)electrochemical conditions. (a) α-Fe_2O_3(0001)-4*OH & 4*H_{sub}, (b) α-Fe_2O_3(0001)-4*OH, (c) α-Fe_2O_3(0001)-8*OH, (d) α-Fe_2O_3(0001)-4*OH & 4*O, (e) α-Fe_2O_3(0001)-12*O. Note that the subscript "sub" indicates that the corresponding adsorbates are adsorbed to oxygen atoms in the second layer of the surface. Color code: gold, red, and white denote iron, oxygen, and hydrogen atoms, respectively.

Table 1 OER mechanisms on five different surface configurations of α-Fe_2O_3(0001), indicating whether the active Fe site catalyzes the elementary steps *via* a single branch, double branch, or triple branch

Surface coverage configuration	Single branch	Double branch	Triple branch
α-Fe_2O_3(0001)-4*OH & 4*H_{sub}	✓	✓	✗
α-Fe_2O_3(0001)-4*OH	✓	✓	✗
α-Fe_2O_3(0001)-8*OH	✗	✓	✗
α-Fe_2O_3(0001)-4*OH & 4*O	✗	✓	✗
α-Fe_2O_3(0001)-12*O	✗	✗	✓

3.2 Mechanistic analysis of the OER over the α-Fe_2O_3(0001)-4*OH & 4*H_{sub} surface

For the 4*OH & 4*H_{sub} surface, the OER can proceed *via* a single or a double branch at the active Fe site (*cf.* Table 1). The free-energy changes for the elementary reaction steps of the various single-site and dual-site OER mechanisms (*cf.* eqn (1)–(31) in Section 2) are compiled in Tables S3 and S4 for a single branch and a double branch, respectively. Knowledge of the free-energy changes enables the construction of free-energy diagrams along the reaction coordinate, which are analyzed at $U = 1.53$ V *vs.* RHE (*cf.* Fig. 5). We observe that the mononuclear mechanism is the preferred pathway for the OER on a single branch, quantified by $G_{max}(U = 1.53\ V) = 0.50$ eV. The limiting free-energy span corresponds to the formation of gaseous oxygen (O_2), indicating that the transition from the *OH intermediate to $O_{2(g)}$ is uphill in free energy. A different situation is encountered for the OER on a double branch. There, the oxide mechanism corresponds to the preferred mechanistic description, with $G_{max}(U = 1.53\ V) = 0.45$ eV. The limiting free-energy span is also related to the formation of gaseous oxygen, although O_2 is formed by a chemical step based on the conversion of the intermediate *OO + *OO into *O + *O. While the intrinsic activity of the double-branch Fe site is slightly higher than that of the single-branch Fe site due to a smaller $G_{max}(U = 1.53\ V)$ value, it should be noted that the potential dependence of the limiting free-energy spans is different. Therefore, the single-branch Fe site is identified as the main active site for larger anodic overpotentials.

3.3 Mechanistic analysis of the OER over the α-Fe_2O_3(0001)-4*OH surface

For the 4*OH surface, the OER can proceed *via* a single or a double branch at the active Fe site (*cf.* Table 1). The free-energy changes for the elementary reaction steps of the various single-site and dual-site OER mechanisms (*cf.* eqn (1)–(31) in Section 2) are compiled for the single and double branches in Tables S5 and S6, respectively. Knowledge of the free-energy changes enables the construction of free-energy diagrams along the reaction coordinate, which are analyzed at $U = 1.53$ V *vs.* RHE (*cf.* Fig. 6). Both the mononuclear and mononuclear-Walden pathways are the preferred mechanistic descriptions for the OER on a single branch, quantified by $G_{max}(U = 1.53\ V) = 0.62$ eV. The limiting free-energy span corresponds to the conversion of the *OH to the *O intermediate in both pathways (*cf.* Fig. 6a). For the double-branch active Fe site, the mononuclear-Walden mechanism becomes the preferred mechanistic description, with $G_{max}(U = 1.53\ V) = 0.50$ eV. The limiting free-energy span also corresponds to the formation of the *O intermediate. Please note that the spectator *OH adsorbate at the active site can form a hydrogen bond with the oxygen atoms of some of the intermediates in the OER mechanisms (*cf.* Fig. S56 in Section S8 of the SI). This contributes to

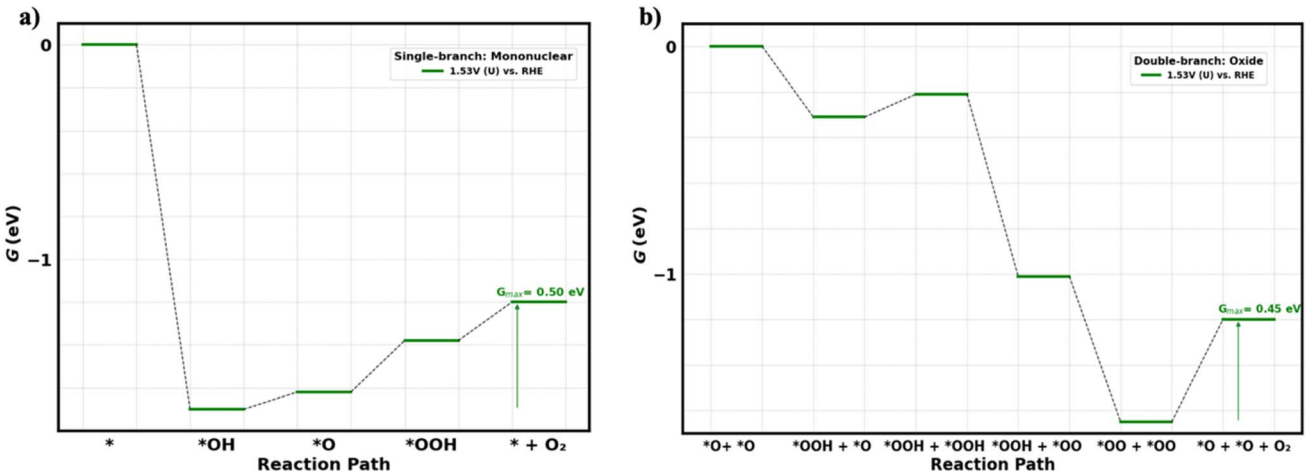

Fig. 5 Energetically favored mechanisms of the OER on the α-Fe_2O_3(0001)-4*OH & 4*H_{sub} surface: (a) single-branch active Fe site, (b) double-branch active Fe site. The green arrow indicates the limiting free-energy span in the approximation of the descriptor $G_{max}(U)$ at $U = 1.53$ V *vs.* RHE. Detailed potential-dependent free-energy diagrams for all pathways on a single-branch or double-branch Fe site are provided in Fig. S7–S20 (*cf.* Section S7.1 of the SI).

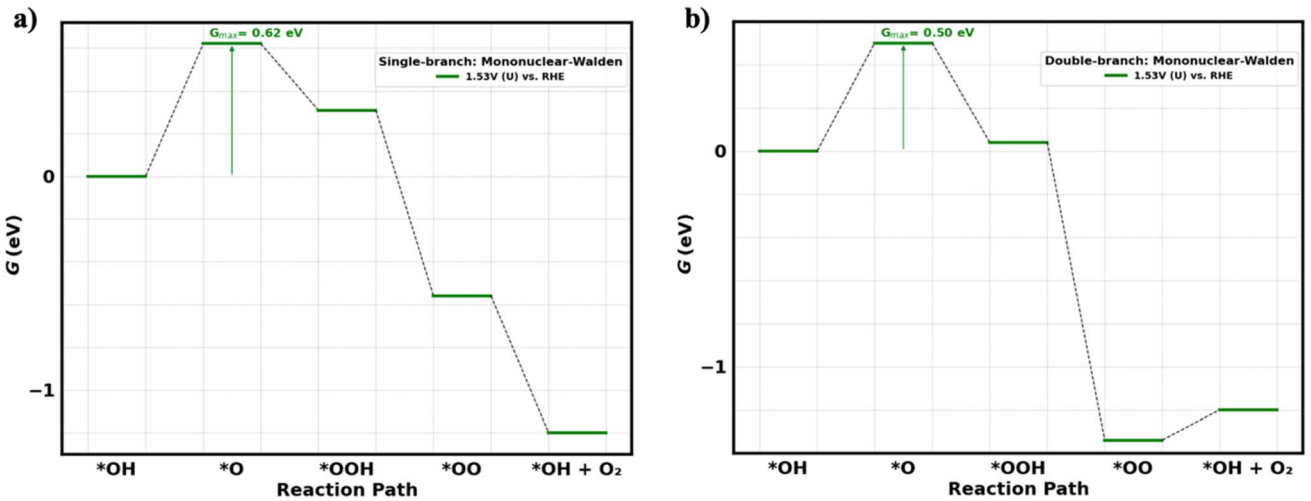

Fig. 6 Energetically favored mechanisms of the OER on the α-Fe_2O_3(0001)-4*OH surface: (a) single-branch active Fe site, (b) double-branch active Fe site. The green arrow indicates the limiting free-energy span in the approximation of the descriptor $G_{max}(U)$ at $U = 1.53$ V *vs.* RHE. Detailed potential-dependent free-energy diagrams for all pathways on a single branch or double branch Fe site are provided in Fig. S21–S34 (*cf.* Section S7.2 of the SI). Please note that the mononuclear and mononuclear-Walden mechanisms for the single-branch active Fe site reveal the same activity in the approximation of the $G_{max}(U)$ descriptor. Only the mononuclear-Walden description is shown in panel (a).

the stabilization of the reaction intermediates and reduces the $G_{max}(U = 1.53\ V)$ value by 0.12 eV compared to the single-branch active Fe site.

3.4 Mechanistic analysis of the OER over the α-Fe_2O_3(0001)-8*OH surface

For the 8*OH surface, the OER proceeds *via* a double branch at the active Fe site (*cf.* Table 1). The free-energy changes for the elementary reaction steps of the various single-site and dual-site OER mechanisms (*cf.* eqn (1)–(31) in Section 2) are compiled in Table S7. Knowledge of the free-energy changes enables the construction of free-energy diagrams along the reaction coordinate, which are analyzed at $U = 1.53$ V *vs.* RHE (*cf.* Fig. 7). Similar to the 4*OH surface, the mononuclear-Walden pathway is the preferred pathway for OER, with $G_{max}(U = 1.53\ V) = 0.42$ eV. The limiting free-energy span corresponds to the formation of the *O intermediate. Other OER mechanisms on this surface configuration exhibit higher $G_{max}(U)$ values, as summarized in Table S14.

3.5 Mechanistic analysis of the OER over the α-Fe_2O_3(0001)-4*OH & 4*O surface

For the 4*OH & 4*O surface, the OER proceed *via* a double branch at the active Fe site (*cf.* Table 1). While this surface is not part of the Pourbaix diagram (*cf.* Fig. S6), it is energetically only slightly less stable than the other four surface configurations (*cf.*

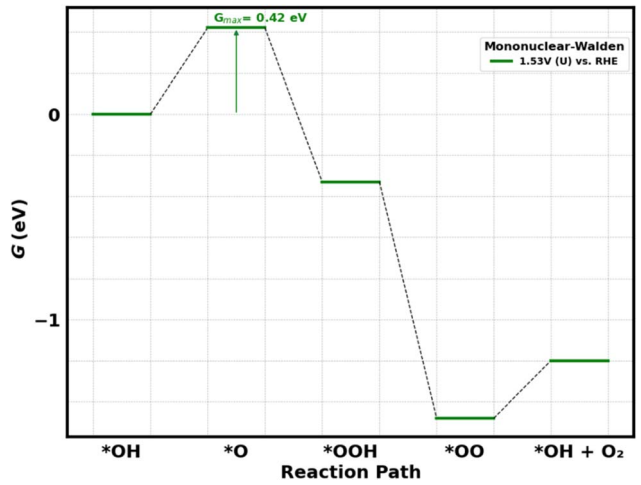

Fig. 7 Energetically favored mechanism of the OER on the α-Fe_2O_3(0001)-8*OH surface. The green arrow indicates the limiting free-energy span in the approximation of the descriptor $G_{max}(U)$ at U = 1.53 V *vs.* RHE. Detailed potential-dependent free-energy diagrams for all pathways are provided in Fig. S35–S41 (*cf.* Section S7.3 of the SI).

Fig. 4), which motivates to include this phase when sampling different surface structures under OER conditions. The free-energy changes for the elementary reaction steps of the various single-site and dual-site OER mechanisms (*cf.* eqn (1)–(31) in Section 2) are compiled in Table S8. Free-energy diagrams along the reaction coordinate reveal that the mononuclear-Walden pathway corresponds to the preferred mechanism at U = 1.53 V *vs.* RHE (*cf.* Fig. 8). The limiting free-energy span related to $G_{max}(U = 1.53\ V) = 0.54$ eV corresponds to the so-called Walden step, in which the formation of gaseous oxygen and the simultaneous adsorption of water to form the *OH intermediate occur in a concerted manner. Compared to the fully hydroxylated surface (8*OH), the $G_{max}(U$ = 1.53 V) value for the partially hydroxylated surface (4*OH & 4*O) is 0.12 eV higher. This finding suggests that the partially hydroxylated surface coverage may have lower OER activity than the fully hydroxylated surface, although the difference of 0.12 eV in $G_{max}(U)$ is within the sensitivity range of this descriptor.

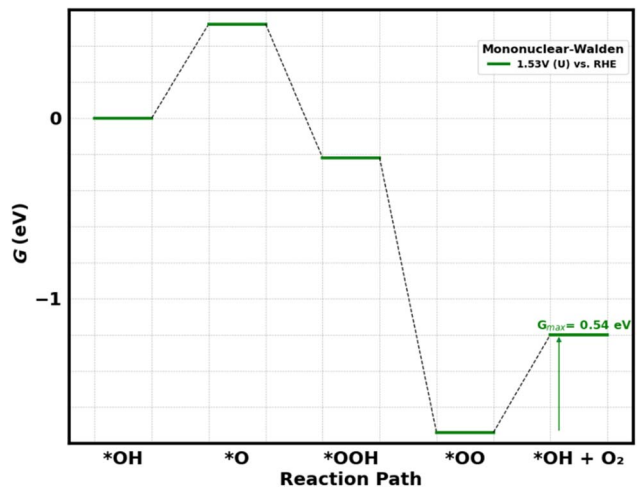

Fig. 8 Energetically favored mechanism of the OER on the α-Fe_2O_3(0001)-4*OH & 4*O surface. The green arrow indicates the limiting free-energy span in the approximation of the descriptor $G_{max}(U)$ at U = 1.53 V *vs.* RHE. Detailed potential-dependent free-energy diagrams for all pathways are provided in Fig. S42–S48 (*cf.* Section S7.4 of the SI).

3.6 Mechanistic analysis of the OER over the α-Fe_2O_3(0001)-12*O surface

For the 12*O (fully oxygen-covered) surface, the OER proceeds *via* a triple branch at the active Fe site (*cf.* Table 1). The photoelectrochemical operating condition under solar illumination (U = 2.30 V *vs.* RHE) are within the stability range of this surface configuration. For consistency and to compare the energetics to the other surface phases, we analyze the elementary steps of OER on the fully oxygen-covered hematite surface at U = 1.53 V *vs.* RHE. The free-energy changes for the elementary reaction steps of the various single-site and dual-site OER mechanisms (*cf.* eqn (1)–(31) in Section 2) are compiled in Table S9. Knowledge of the free-energy changes enables the construction of free-energy diagrams along the reaction coordinate (*cf.* Fig. 9), where the bifunctional-Walden pathway is identified as the preferred OER pathway, quantified by $G_{max}(U$ = 1.53 V) = 0.34 eV. The limiting free-energy span corresponds to the Walden step, which involves the release of gaseous oxygen with adsorption and oxidation of a water molecule (*cf.* Fig. 9).

3.7 Discussion

In this work, we investigate the (photo-)electrochemical OER on the Fe–O–Fe– termination of α-Fe_2O_3(0001) for different surface coverages using DFT calculations. First, we note that different surface configurations turn out to be stable in dependence of the applied electrode potential (*cf.* Fig. S6). While photoelectrochemical conditions refer to U = 2.30 V *vs.* RHE,[6,7,12] we analyze the elementary steps at U = 1.53 V *vs.* RHE

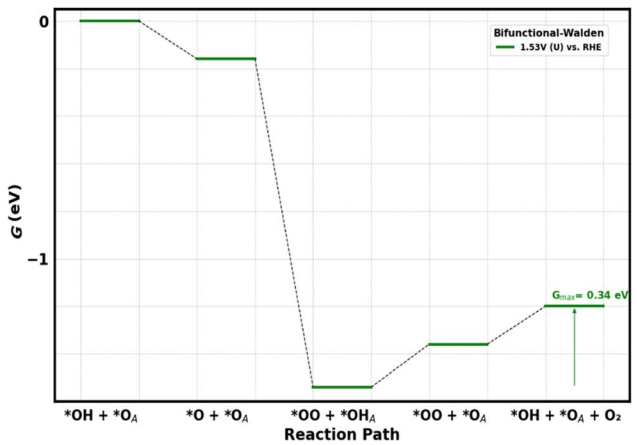

Fig. 9 Energetically favored mechanism of the OER on the α-Fe_2O_3(0001)-12*O surface. The green arrow indicates the limiting free-energy span in the approximation of the descriptor $G_{max}(U)$ at U = 1.53 V *vs.* RHE. Detailed potential-dependent free-energy diagrams for all pathways are provided in Fig. S49–S55 (*cf.* Section S7.5 of the SI).

to maintain consistency across the different surface phases. In this context, it must be emphasized that the energetics of the elementary steps for all surface configurations is downhill in free energy at $U = 2.30$ V *vs.* RHE, which does not allow a meaningful comparison under these potential conditions. To this end, we use a descriptor-based analysis at an applied overpotential of 300 mV for OER, which is a common approach in the community following previous work on this topic.[35,37,81,82] In this analysis, we do not explicitly account for the effects of photogenerated electron–hole pairs; for an in-depth discussion, readers are referred to Peter's work.[83]

Previous computational studies have shown that the Fe–O–Fe– termination of hematite, although the most thermodynamically stable termination, is inactive for OER and that its catalytic activity for OER is instead related to the Fe–Fe–O– termination.[10,12,13] We challenge this finding in the present article by demonstrating that the Fe–O–Fe– termination of hematite is sufficiently active for OER based on our dedicated analysis (*cf.* Sections 3.2–3.6). We attribute the difference in results to the omission of relevant mechanistic OER pathways in previous studies, underpinning that the mechanistic complexity of the four-proton coupled electron transfer steps is relevant for activity predictions using electronic structure theory in the DFT framework.

Although our main results differ from previous studies as we have enormously expanded the parameter space regarding OER mechanisms and different surface coverages of hematite, we emphasize that our results are nevertheless consistent with previous work: adopting the fully oxygen-covered α-Fe_2O_3(0001) as an example, the mononuclear mechanism over this surface configuration reveals a thermodynamic overpotential of 1.82 V, indicating that this mechanism is inactive for OER. This finding is in qualitative agreement with the results reported by Nguyen *et al.* or Hajiyani and Pentcheva.[10,12] On the other hand, a bifunctional-Walden pathway on the α-Fe_2O_3(0001)-12*O surface reveals a significantly lower thermodynamic overpotential of 0.48 V, which corresponds to $G_{max}(U = 1.53\ V) = 0.34$ eV (*cf.* Fig. 9) and indicates high OER activity. Importantly, the inclusion of Walden mechanisms in the OER significantly influences activity predictions and this finding is not limited to the fully oxygen-covered surface. Transition state calculations for Walden-type steps were performed in previous works on IrO_2 (ref. 65) and single-atom centers of MXenes.[37] Walden-type steps are kinetically not impeded compared to conventional O_2 desorption steps. Therefore, we conclude that the Walden-type steps are likely kinetically not restricted on the Fe–O–Fe– termination of hematite.

Fig. 10 compares the different surface coverages and the different active Fe sites. It is noteworthy that in five out of seven cases, a Walden pathway corresponds to the favorable mechanistic description of OER, while the conventional OER mechanism is observed only in two cases. This finding underlines that considering a traditional mononuclear mechanism alone is not sufficient for the theoretical description of hematite-based materials under (photo-)electrochemical conditions.

While the 12*O coverage with a triple-branch Fe active site reveals the lowest $G_{max}(U = 1.53\ V)$ value, we find that the $G_{max}(U)$ values differ by a maximum of 0.30 eV, which is almost within the sensitivity range of this descriptor.[67] Therefore, we conclude that different surface coverages do not lead to a strong modulation of the electrocatalytic activity for α-Fe_2O_3(0001), although there is some tendency that higher coverages and OER on double- or triple-branch motifs lead to higher OER activity.

For the materials science community, it is important to emphasize that the development of improved materials composition of hematite for OER was mainly based on the thermodynamically less stable Fe–Fe–O– termination.[6,10,12,13] The present work provides a new direction for the development of (photo-)electrochemical OER catalysts by exploiting the stable Fe–O–Fe– termination of hematite as a starting point for screening dopants,[10,13,18,22,26,27,84–86] strain engineering,[87,88] introducing defects,[29,89] or other approaches. The use of the most

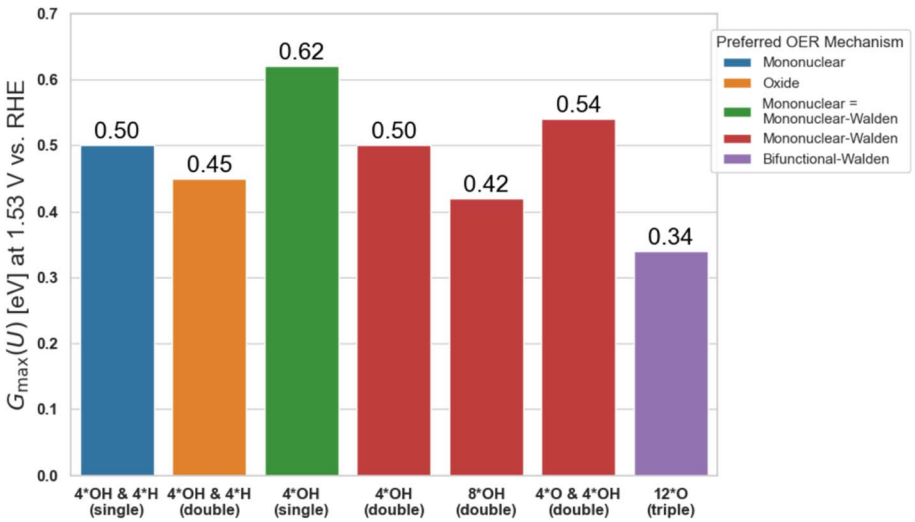

Fig. 10 Summary of the preferred OER mechanisms and their $G_{max}(U = 1.53\ V)$ values for different surface coverages of the Fe–O–Fe– termination of hematite. Below each bar, the surface coverage and branching at the active Fe site are indicated.

Table 2 Comparison of thermodynamic overpotentials (η_{TD}) for OER in dependence of the preferred reaction mechanisms for the most stable Fe–O–Fe– termination and less stable Fe–Fe–O– termination of hematite. Different surface coverages are highlighted in parentheses

Termination (surface coverages)-branch	OER mechanism	η_{TD} (V)
Fe–O–Fe–(4*OH & 4*H_{sub})-single	Mononuclear	0.54 (this work)
Fe–O–Fe–(4*OH & 4*H_{sub})-double	Oxide	0.40 (this work)
Fe–O–Fe–(4*OH)-single	Mononuclear-Walden	0.92 (this work)
Fe–O–Fe–(4*OH)-double	Mononuclear-Walden	0.80 (this work)
Fe–O–Fe–(8*OH)-double	Mononuclear-Walden	0.72 (this work)
Fe–O–Fe–(4*OH & 4*O)-double	Mononuclear-Walden	0.84 (this work)
Fe–O–Fe–(12*O)-double	Bifunctional-Walden	0.48 (this work)
Fe–O–Fe–(O)	Mononuclear	1.22 (ref. 12)
Fe–O–Fe–(H_2O)	Mononuclear	1.12 (ref. 10)
Fe–Fe–O–	Mononuclear	0.84 (ref. 12)
Fe–Fe–O–	Mononuclear	0.81 (ref. 10)
Fe–Fe–O–(H)	Mononuclear	0.56 (ref. 10)
Fe–Fe–O–	Mononuclear	0.82 (ref. 6)
Fe–Fe–O–	Mononuclear	0.77 (ref. 13)

stable Fe–O–Fe– termination instead of Fe–Fe–O– termination may also be beneficial to improve the stability of hematite under the harsh anodic conditions of OER, although a discussion of catalyst stability is beyond the scope of this contribution.

Our literature survey assessed the activity of the Fe–O–Fe– and Fe–Fe–O– terminations using the thermodynamic overpotential (η_{TD}) as the activity descriptor, with values taken from ref. 6, 10, 12 and 13. These literature values were then compared with the η_{TD} values for various surface coverages of the Fe–O–Fe– termination obtained from our simulations, as summarized in Table 2.

We note that the η_{TD} values of the Fe–O–Fe– terminations are smaller than those of the Fe–Fe–O– terminations. We do not aim to interpret this finding, as an unbiased comparison is not possible: we have used seven different mechanisms for the description of OER on the Fe–O–Fe– termination, while previous literature works relied on a single mechanism. However, qualitatively speaking, catalysts with η_{TD} < 1 V are often considered to be active for photoelectrochemical water splitting. Table 2 illustrates that this criterion is already fulfilled for the less stable Fe–Fe–O– termination, whereas only the present work reports that the Fe–O–Fe– termination reveals η_{TD} < 1 V for Walden-type mechanisms.

4 Conclusions

In the present work, we utilized electronic structure calculations in the density functional theory framework to investigate various reaction mechanisms for oxygen evolution (OER) on the Fe–O–Fe– termination of α-Fe_2O_3(0001) using a combination of surface Pourbaix diagrams, free-energy diagrams, and descriptor-based analysis. We demonstrate that reliance on a single OER mechanism can lead to incorrect conclusions regarding the electrocatalytic activity of hematite-based materials. In particular, the high electrocatalytic activity of the Fe–O–Fe– termination is ascribed to Walden-type mechanisms, where the desorption of the product O_2 is accompanied with the adsorption and oxidation of water on the hematite surface. The omission of Walden-type pathways in previous computational studies explains why previous work put forth the less stable Fe–Fe–O– termination of hematite for (photo-)electrochemical water splitting. The present work could change this view, and we propose to exploit the most stable Fe–O–Fe– termination of hematite for the development of (photo-)electrochemical OER catalysts through doping, strain, or defect engineering.

Author contributions

Shinie S. Awulachew: conceptualization, formal analysis, investigation, data curation, visualization, validation, writing – original draft, writing – review & editing, funding acquisition. Kapil Dhaka: conceptualization, validation, writing – review & editing. Ebrahim Tayyebi: conceptualization, validation, writing – review & editing. Kai S. Exner: conceptualization, methodology, resources, validation, writing – original draft, writing – review & editing, supervision, project administration.

Conflicts of interest

There are no conflicts to declare.

Data availability

The data supporting this article have been included as part of the SI. See DOI: https://doi.org/10.1039/d5ta04755b.

Acknowledgements

SSA acknowledges the German Academic Exchange Service (DAAD) scholarship and International Max Planck Research School for Sustainable Metallurgy (IMPRS SusMet) for the financial support to carry out this study. KD and KSE acknowledge funding from the CRC/TRR247: "Heterogeneous Oxidation Catalysis in the Liquid Phase" (Project number 388390466-TRR 247). ET and KSE acknowledge funding by the Ministry of Culture and Science of the Federal State of North Rhine-Westphalia (NRW return grant). KSE further acknowledges funding by the Deutsche Forschungsgemeinschaft

through the RESOLV Cluster of Excellence (EXC 2033 – 390677874 – RESOLV).

References

1 M. Chatenet, B. G. Pollet, D. R. Dekel, F. Dionigi, J. Deseure, P. Millet, R. D. Braatz, M. Z. Bazant, M. Eikerling, I. Staffell, P. Balcombe, Y. Shao-Horn and H. Schäfer, *Chem. Soc. Rev.*, 2022, **51**, 4583–4762.
2 K. Sivula, F. Le Formal and M. Grätzel, *ChemSusChem*, 2011, **4**, 432–449.
3 A. B. Murphy, P. R. F. Barnes, L. K. Randeniya, I. C. Plumb, I. E. Grey, M. D. Horne and J. A. Glasscock, *Int. J. Hydrogen Energy*, 2006, **31**, 1999–2017.
4 R. M. Cornell and U. Schwertmann, in *The Iron Oxides*, 2003, DOI: 10.1002/3527602097.
5 A. Kleiman-Shwarsctein, Y. S. Hu, A. J. Forman, G. D. Stucky and E. W. McFarland, *J. Phys. Chem. C*, 2008, **112**, 15900–15907.
6 K. Ulman, M. T. Nguyen, N. Seriani, S. Piccinin and R. Gebauer, *ACS Catal.*, 2017, **7**, 1793–1804.
7 A. Hellman and R. G. S. Pala, *J. Phys. Chem. C*, 2011, **115**, 12901–12907.
8 X. Zhang, C. Cao and A. Bieberle-Hütter, *J. Phys. Chem. C*, 2016, **120**, 28694–28700.
9 N. Seriani, *J. Phys.: Condens. Matter*, 2017, **29**, 463002.
10 H. Hajiyani and R. Pentcheva, *J. Chem. Phys.*, 2020, **152**, 124709.
11 J. Noh, H. Li, O. I. Osman, S. G. Aziz, P. Winget and J. L. Brédas, *Adv. Energy Mater.*, 2018, **8**, 1800545.
12 M. T. Nguyen, N. Seriani, S. Piccinin and R. Gebauer, *J. Chem. Phys.*, 2014, **140**, 064703.
13 P. Liao, J. A. Keith and E. A. Carter, *J. Am. Chem. Soc.*, 2012, **134**, 13296–13309.
14 S. Xu, J. Yang, P. Su, Q. Wang, X. Yang, Z. Zhou and Y. Li, *Nat. Commun.*, 2024, **15**(1), 1–12.
15 A. Kay, I. Cesar and M. Grätzel, *J. Am. Chem. Soc.*, 2006, **128**, 15714–15721.
16 Y. Zhang, H. Zhang, A. Liu, C. Chen, W. Song and J. Zhao, *J. Am. Chem. Soc.*, 2018, **140**, 3264–3269.
17 N. Yatom, O. Neufeld and M. Caspary Toroker, *J. Phys. Chem. C*, 2015, **119**, 24789–24795.
18 M. C. Toroker, *J. Phys. Chem. C*, 2014, **118**, 23162–23167.
19 B. Iandolo and A. Hellman, *Angew. Chem., Int. Ed.*, 2014, **53**, 13404–13408.
20 S. C. Warren, K. Voïtchovsky, H. Dotan, C. M. Leroy, M. Cornuz, F. Stellacci, C. Hébert, A. Rothschild and M. Grätzel, *Nat. Mater.*, 2013, **12**(9), 842–849.
21 Z. Jakub, M. Meier, F. Kraushofer, J. Balajka, J. Pavelec, M. Schmid, C. Franchini, U. Diebold and G. S. Parkinson, *Nat. Commun.*, 2021, **12**(1), 1–8.
22 J. Redondo, M. Reticcioli, V. Gabriel, D. Wrana, F. Ellinger, M. Riva, G. Franceschi, E. Rheinfrank, I. Sokolović, Z. Jakub, F. Kraushofer, A. Alexander, E. Belas, L. L. Patera, J. Repp, M. Schmid, U. Diebold, G. S. Parkinson, C. Franchini, P. Kocan and M. Setvin, Real-space investigation of polarons in hematite Fe_2O_3, *Sci. Adv.*, 2024, **10**, eadp7833.
23 A. J. Bosman, H. J. van Daal, A. J. Bosman and H. J. van Daal, *Adv. Phys.*, 1970, **19**, 1–117.
24 N. Iordanova, M. Dupuis and K. M. Rosso, *J. Chem. Phys.*, 2005, **122**, 144305.
25 N. J. Cherepy, D. B. Liston, J. A. Lovejoy, H. Deng and J. Z. Zhang, *J. Phys. Chem. B*, 1998, **102**, 770–776.
26 S. Shen, C. X. Kronawitter, D. A. Wheeler, P. Guo, S. A. Lindley, J. Jiang, J. Z. Zhang, L. Guo and S. S. Mao, *J. Mater. Chem. A*, 2013, **1**, 14498–14506.
27 K. Y. Yoon, J. Park, H. Lee, J. H. Seo, M. J. Kwak, J. H. Lee and J. H. Jang, *ACS Catal.*, 2022, **12**, 5112–5122.
28 S. Yin, X. Ma and D. E. Ellis, *Surf. Sci.*, 2007, **601**, 2426–2437.
29 R. B. Wang and A. Hellman, *J. Phys. Chem. C*, 2019, **123**, 2820–2827.
30 P. Liu, T. Kendelewicz, G. E. Brown, E. J. Nelson and S. A. Chambers, *Surf. Sci.*, 1998, **417**, 53–65.
31 T. P. Trainor, A. M. Chaka, P. J. Eng, M. Newville, G. A. Waychunas, J. G. Catalano and G. E. Brown, *Surf. Sci.*, 2004, **573**, 204–224.
32 I. C. Man, H. Y. Su, F. Calle-Vallejo, H. A. Hansen, J. I. Martínez, N. G. Inoglu, J. Kitchin, T. F. Jaramillo, J. K. Nørskov and J. Rossmeisl, *ChemCatChem*, 2011, **3**, 1159–1165.
33 K. S. Exner, *Mater. Horiz.*, 2023, **10**, 2086–2095.
34 K. S. Exner, *Adv. Sci.*, 2023, **10**, 2305505.
35 K. Dhaka and K. S. Exner, *J. Catal.*, 2025, **443**, 115970.
36 S. Kozuch and S. Shaik, *Acc. Chem. Res.*, 2011, **44**, 101–110.
37 S. Razzaq, S. Faridi, S. Kenmoe, M. Usama, D. Singh, L. Meng, F. Vines, F. Illas and K. S. Exner, *J. Am. Chem. Soc.*, 2025, **147**, 161–168.
38 S. Yu, Z. Levell, Z. Jiang, X. Zhao and Y. Liu, *J. Am. Chem. Soc.*, 2023, **145**, 25352–25356.
39 G. Kresse and J. Hafner, *Phys. Rev. B: Condens. Matter Mater. Phys.*, 1993, **47**, 558–561.
40 G. Kresse and J. Furthmüller, *Comput. Mater. Sci.*, 1996, **6**, 15–50.
41 G. Kresse and J. Furthmüller, *Phys. Rev. B: Condens. Matter Mater. Phys.*, 1996, **54**, 11169–11186.
42 A. Kiejna and T. Pabisiak, *J. Phys.: Condens. Matter*, 2012, **24**, 095003.
43 P. Liao and E. A. Carter, *Phys. Chem. Chem. Phys.*, 2011, **13**, 15189–15199.
44 M. T. Nguyen, N. Seriani and R. Gebauer, *J. Chem. Phys.*, 2024, **140**, 064703.
45 K. Mathew, R. Sundararaman, K. Letchworth-Weaver, T. A. Arias and R. G. Hennig, *J. Chem. Phys.*, 2014, **140**, 084106.
46 J. P. Perdew, K. Burke and M. Ernzerhof, *Phys. Rev. Lett.*, 1996, **77**, 3865.
47 M. Cococcioni and S. De Gironcoli, *Phys. Rev. B: Condens. Matter Mater. Phys.*, 2005, **71**, 035105.
48 S. Grimme, J. Antony, S. Ehrlich and H. Krieg, *J. Chem. Phys.*, 2010, **132**, 154104.
49 L. Bengtsson, *Phys. Rev. B: Condens. Matter Mater. Phys.*, 1999, **59**, 12301–12304.

50 G. Kresse and D. Joubert, *Phys. Rev. B: Condens. Matter Mater. Phys.*, 1999, **59**, 1758.
51 A. Hjorth Larsen, J. JØrgen Mortensen, J. Blomqvist, I. E. Castelli, R. Christensen, M. Dułak, J. Friis, M. N. Groves, B. Hammer, C. Hargus, E. D. Hermes, P. C. Jennings, P. Bjerre Jensen, J. Kermode, J. R. Kitchin, E. Leonhard Kolsbjerg, J. Kubal, K. Kaasbjerg, S. Lysgaard, J. Bergmann Maronsson, T. Maxson, T. Olsen, L. Pastewka, A. Peterson, C. Rostgaard, J. SchiØtz, O. Schütt, M. Strange, K. S. Thygesen, T. Vegge, L. Vilhelmsen, M. Walter, Z. Zeng and K. W. Jacobsen, *J. Phys.: Condens. Matter*, 2017, **29**, 273002.
52 K. Momma and F. Izumi, *J. Appl. Crystallogr.*, 2011, **44**, 1272–1276.
53 M. Sokolov, Y. A. Mastrikov, D. Bocharov, V. Krasnenko, G. Zvejnieks, K. S. Exner and E. A. Kotomin, *Catal. Today*, 2024, **432**, 114609.
54 J. Rossmeisl, A. Logadottir and J. K. Nørskov, *Chem. Phys.*, 2005, **319**, 178–184.
55 J. Rossmeisl, Z. W. Qu, H. Zhu, G. J. Kroes and J. K. Nørskov, *J. Electroanal. Chem.*, 2007, **607**, 83–89.
56 F. Hess and H. Over, *ACS Catal.*, 2023, **13**, 3433–3443.
57 M. A. W. Schoen, O. Calderon, N. M. Randell, S. Jimenez-Villegas, K. M. Daly, R. Chernikov and S. Trudel, *J. Mater. Chem. A*, 2021, **9**, 13252–13262.
58 N. B. Halck, V. Petrykin, P. Krtil and J. Rossmeisl, *Phys. Chem. Chem. Phys.*, 2014, **16**, 13682–13688.
59 H. N. Nong, L. J. Falling, A. Bergmann, M. Klingenhof, H. P. Tran, C. Spöri, R. Mom, J. Timoshenko, G. Zichittella, A. Knop-Gericke, S. Piccinin, J. Pérez-Ramírez, B. R. Cuenya, R. Schlögl, P. Strasser, D. Teschner and T. E. Jones, *Nature*, 2020, **587**, 408–413.
60 Y. H. Fang and Z. P. Liu, *J. Am. Chem. Soc.*, 2010, **132**, 18214–18222.
61 Y. Ping, R. J. Nielsen and W. A. Goddard, *J. Am. Chem. Soc.*, 2017, **139**, 149–155.
62 M. Busch, E. Ahlberg and I. Panas, *Phys. Chem. Chem. Phys.*, 2011, **13**, 15069–15076.
63 M. Busch, *Curr. Opin. Electrochem.*, 2018, **9**, 278–284.
64 T. Binninger and M. L. Doublet, *Energy Environ. Sci.*, 2022, **15**, 2519–2528.
65 M. Usama, S. Razzaq, C. Hättig, S. N. Steinmann and K. S. Exner, *Nat. Commun.*, 2025, **16**(1), 1–13.
66 J. K. Nørskov, J. Rossmeisl, A. Logadottir, L. Lindqvist, J. R. Kitchin, T. Bligaard and H. Jónsson, *J. Phys. Chem. B*, 2004, **108**, 17886–17892.
67 K. S. Exner, *ACS Catal.*, 2020, **10**, 12607–12617.
68 S. Razzaq and K. S. Exner, *ACS Catal.*, 2023, **13**, 1740–1758.
69 M. Usama, S. Razzaq and K. S. Exner, *ACS Phys. Chem. Au*, 2025, **5**, 38–46.
70 O. van der Heijden, S. Park, R. E. Vos, J. J. J. Eggebeen and M. T. M. Koper, *ACS Energy Lett.*, 2024, **9**, 1871–1879.
71 T. Shinagawa, A. T. Garcia-Esparza and K. Takanabe, *Sci. Rep.*, 2015, **5**(1), 1–21.
72 K. S. Exner, *Acc. Chem. Res.*, 2024, **57**, 1336–1345.
73 W. Schmickler and S. Trasatti, *J. Electrochem. Soc.*, 2006, **153**, L31.
74 N. Govindarajan, J. M. García-Lastra, E. J. Meijer and F. Calle-Vallejo, *Curr. Opin. Electrochem.*, 2018, **8**, 110–117.
75 M. J. Craig and M. García-Melchor, *Curr. Opin. Electrochem.*, 2022, **35**, 101044.
76 A. Rohrbach, J. Hafner and G. Kresse, *Phys. Rev. B: Condens. Matter Mater. Phys.*, 2004, **70**, 125426.
77 S. M. O. Souvi, M. Badawi, J. F. Paul, S. Cristol and L. Cantrel, *Surf. Sci.*, 2013, **610**, 7–15.
78 H. A. Hansen, J. Rossmeisl and J. K. Nørskov, *Phys. Chem. Chem. Phys.*, 2008, **10**, 3722–3730.
79 A. M. Verma, L. Laverdure, M. M. Melander and K. Honkala, *ACS Catal.*, 2022, **12**, 662–675.
80 A. Groß, *Curr. Opin. Electrochem.*, 2021, **27**, 100684.
81 S. Faridi, S. Razzaq, D. Singh, L. Meng, F. Viñes, F. Illas and K. S. Exner, *J. Mater. Chem. A*, 2025, **13**, 16481–16490.
82 S. Singh and N. Karmodak, *ACS Appl. Energy Mater.*, 2024, **7**, 7854–7863.
83 L. M. Peter, *J. Solid State Electrochem.*, 2025, **29**, 2141–2155.
84 J. Kang, K. Y. Yoon, J. E. Lee, J. Park, S. Chaule and J. H. Jang, *Nano Energy*, 2023, **107**, 108090.
85 J. Park, K. Y. Yoon, M. J. Kwak, J. Kang, S. Kim, S. Chaule, S. J. Ha and J. H. Jang, *ACS Appl. Mater. Interfaces*, 2022, **15**, 9341–9349.
86 O. Neufeld and M. C. Toroker, *J. Phys. Chem. C*, 2015, **119**, 5836–5847.
87 T. V. Bogdanova, A. A. Meshcheryakov, D. V. Kalyabin, A. B. Khutieva, A. V. Sadovnikov, A. R. Safin and S. A. Nikitov, *Appl. Phys. Lett.*, 2024, **124**, 92410.
88 D. Singh, K. Bulatova and K. S. Exner, *Chem. Eng. J.*, 2025, **518**, 164451.
89 M. T. Nguyen, S. Piccinin, N. Seriani and R. Gebauer, *ACS Catal.*, 2015, **5**, 715–721.